UV Photofragmentation Dynamics of Acetaldehyde Cations Prepared by Single-Photon VUV Ionization

Kara M. Kapnas,[1] Laura M. McCaslin,[2] and Craig Murray[1,*]

1. *Department of Chemistry, University of California, Irvine, Irvine CA 92697, USA*
2. *The Fritz Haber Center and The Institute of Chemistry, The Hebrew University, Jerusalem 91904, Israel*

[*] Email: craig.murray@uci.edu; Telephone: +1-949-824-4218

Abstract

Acetaldehyde cations (CH_3CHO^+) were prepared using single-photon vacuum ultraviolet ionization of CH_3CHO in a molecular beam and the fragmentation dynamics explored over the photolysis wavelength range 390–210 nm using velocity-map ion imaging and photofragment yield (PHOFY) spectroscopy. Four fragmentation channels are characterized:

$$CH_3CHO^+ \rightarrow C_2H_3O^+ + H \quad \text{I}$$

$$CH_3CHO^+ \rightarrow HCO^+ + CH_3 \quad \text{II}$$

$$CH_3CHO^+ \rightarrow CH_3^+ + HCO \quad \text{III}$$

$$CH_3CHO^+ \rightarrow CH_4^+ + CO \quad \text{IV}$$

Channels I, II, and IV are observed across the full photolysis wavelength range while channel III is observed only at $\lambda < 317$ nm. Maximum fragment ion yields are obtained at ~250 nm. Ion images were recorded over the range 316–228 nm, which corresponds to initial excitation to the $\tilde{B}^2A'$ and $\tilde{C}^2A'$ states of CH_3CHO^+. The speed and angular distributions are distinctly different for each detected ion and show evidence of both statistical and dynamical fragmentation pathways. At longer wavelengths, fragmentation via channel I leads to modest translational energies (E_T), consistent with dissociation over a small barrier and production of highly internally excited CH_3CO^+. Additional components with E_{INT} greater than the CH_3CO^+ secondary dissociation threshold appear at shorter wavelengths and are assigned to fragmentation products of vinyl alcohol cation or oxirane cation formed by isomerization of energized CH_3CHO^+. The E_T distribution observed for channel III products peaks at zero but is notably colder than that predicted by phase space theory, particularly at longer photolysis wavelengths. The colder-than-statistical E_T distributions are attributed to contributions from secondary fragmentation of energized CH_3CO^+ formed via channel I, which are attenuated by CH_3CHO^+ isomerization at shorter wavelengths. Fragmentation via channels II and IV results in

qualitatively similar outcomes, with evidence of isotropic statistical components at low-E_T and anisotropic components due to excited state dynamics at higher E_T.

Introduction

Molecules, radicals, and ions are ubiquitous in interstellar space, with several neutral complex organic molecules (COMs) having been observed.[1] Depending on the interstellar environment, COMs have the potential to be ionized *via* charge transfer reactions or cosmic radiation.[2] The ultraviolet and vacuum ultraviolet (UV and VUV) radiation fields produced by surrounding stars have the potential to both rapidly ionize and dissociate these molecules.[3] One such COM that could be relevant in interstellar space is acetaldehyde cation, CH_3CHO^+, whose neutral counterpart has been detected in numerous interstellar environments.[4–9] The photochemistry of CH_3CHO^+ is consequently of fundamental interest and potential astrochemical relevance.

The photofragmentation dynamics of molecular cations has attracted attention over the last few decades, with velocity-map imaging proving to be a particularly effective tool for detailed examination. Most studies have used resonance-enhanced multiphoton ionization (REMPI) to state-selectively prepare cations, with absorption of an additional photon of the same wavelength inducing fragmentation. Ashfold and co-workers have used this approach to examine the photochemistry of the cations of diatomic halogens and interhalogens,[10–12] alkyl halides,[13] and first-row hydrides.[14,15] Suits and co-workers have examined the photochemistry of several aldehyde,[16–18] amine,[19,20] and alkene cations;[21,22] their work on cation photofragmentation using imaging techniques has been summarized in a mini-review.[23] Single-photon VUV ionization at 118 nm has also been used to prepare acetone cations, with photofragmentation induced by the residual 355 nm radiation used in VUV generation.[24] From a mass spectrometry perspective, polyatomic ions are thought primarily to fragment statistically, according to the quasi-equilibrium theory in which the energy is assumed to be completely randomized among internal degrees of freedom prior to fragmentaion.[25,26] Examples demonstrating the involvement of excited states in the fragmentation of molecular cations are few.[13,15,16,19]

Information about the electronic states and energy-dependent fragmentation of CH_3CHO^+ comes largely from photoelectron spectroscopy and photoelectron/photoion coincidence (PEPICO) measurements. He I and threshold photoelectron spectra of acetaldehyde show an intense, sharp 0-0 band near 10.29 eV,[27–31] indicative of ionization from the non-bonding n_0 (10a′) orbital. Production of vibrationally excited ions is limited to single quanta in the CH_3 deformation/CC stretch (ν_7) and CH bend (ν_6) modes. Several diffuse bands corresponding to various excited states of the cation are observed at higher photoelectron kinetic energies. Only the Ã band at ~13.1 eV shows vibrational structure, with progressions in the CO stretch (ν_4) and CCO bend (ν_{10}) that are consistent with the ejection of an electron from the $\pi_{C=O}$ (2a″) bonding orbital. The B̃ and C̃ bands at ~13.9 eV and 15.2 eV are assigned to ionization from the π_{CH_3}(9a′) and σ_{C-C} (8a′) orbitals, respectively. A summary of the band assignments, characters, and excitation energies as reported in the most recent work by Yencha *et al*.[31] can be found in Table 1.

PEPICO measurements have mapped out breakdown curves showing the fragmentation as a function of VUV wavelength, up to excitation energies ~7 eV above the ionization energy.[29,30] Four major fragmentation channels have been identified in the PEPICO studies:

$$CH_3CHO^+ \rightarrow C_2H_3O^+ + H \qquad \text{I}$$

$$CH_3CHO^+ \rightarrow HCO^+ + CH_3 \qquad \text{II}$$

$$CH_3CHO^+ \rightarrow CH_3^+ + HCO \qquad \text{III}$$

$$CH_3CHO^+ \rightarrow CH_4^+ + CO \qquad \text{IV}$$

Thermodynamic threshold energies and appearance energies for fragmentation channels I–IV are compiled in Table 2 and illustrated in Figure 1. In general, appearance energies are slightly greater than the thermodynamic thresholds. From the onset of the $\tilde{A}^2A''$ band, channels I and II are thought to proceed on the ground state following internal conversion.[29,30] Channel III products have an appearance energy of 14.1 eV, near the onset of the B̃ band in the photoelectron spectrum.[29,30]

Johnson *et al*. suggested that CH_3^+ production resulted from secondary fragmentation of $C_2H_3O^+$, based upon the observation that the $C_2H_3O^+$ translational energy distributions deviated from a simple statistical model when an excess energy > 3.6 eV was reached.[30] Channel IV products $CH_4^+ + CO$ were observed at photon energies greater than 13 eV in the PEPICO studies of Johnson *et al*.[30] and were associated with dissociation on the $\tilde{A}\,^2A''$ surface. Bombach *et al.*[29] did not observe CH_4^+ formation, however.

Photoionization mass spectrometry (PIMS) measurements by Jochims *et al*.[32] identified hydrogen scrambling in the fragments from partially-deuterated isotopologues CD_3CHO and CH_3CDO following excitation using wavelength-tunable synchrotron radiation, consistent with statistical dissociation on the ground state surface. Substantial fragmentation and hydrogen scrambling has also been observed in 2+1 REMPI spectroscopy via the 3s Rydberg state at wavelengths near 360 nm.[33–35] It was concluded that dissociation resulted from excitation of the ion to the $\tilde{B}^2A'$state. Using the same REMPI transition, Lee *et al*.[16] used velocity-map ion imaging to detect the CH_3CO^+, HCO^+, and CH_4^+ ionic fragments, measuring their translational energy and angular distributions. The observations were generally consistent with excitation to the $\tilde{B}^2A'$ state, with dissociation occurring on the ground state surface. The CH_3CO^+ angular distributions required higher order Legendre polynomial terms, indicating that the ionization process resulted in spatial alignment of the CH_3CHO^+ cations prior to dissociation.

In this paper, we present the results of velocity-map ion imaging experiments characterizing the wavelength-dependent photofragmentation dynamics of the acetaldehyde cation, CH_3CHO^+. Production of CH_3CHO^+ by single-photon VUV ionization allows photolysis of the cation to be probed over a broad range of excitation wavelengths, unlike studies that use REMPI to prepare the parent cation, which are restricted by the resonant step. Photofragment ion yield spectra have been recorded over the wavelength range 390–210 nm and branching fractions for the major products $C_2H_3O^+$, HCO^+, CH_3^+, and CH_4^+ have been determined. Ion images characterizing the photodissociation

dynamics have been measured between 228 nm and 316 nm. The images show evidence of both statistical and dynamical fragmentation mechanisms. Comparisons are drawn with previous one-color measurements of CH_3CHO^+ fragmentation using both direct single-photon VUV ionization and REMPI techniques.

Experimental and Computational Methods

The experimental methods were identical to those used in our recent studies of the UV photochemistry of acetaldehyde and acetone,[36,37] combining photofragment ion yield (PHOFY) spectroscopy and velocity-map ion imaging using VUV ionization to detect products. In these experiments, the time ordering of the UV and VUV laser pulses was simply reversed such that acetaldehyde cations are first formed by the VUV ionization pulse and subsequently dissociated by the UV photolysis pulse. Briefly, a molecular beam of CH_3CHO seeded in Ar carrier gas (~30%) was intersected perpendicularly by counter-propagating ionization and photolysis beams. CH_3CHO^+ was prepared by single-photon VUV ionization at a wavelength of 118.2 nm (10.49 eV), which was generated by frequency tripling the 3rd harmonic of a Nd:YAG laser in a static Xe/Ar gas mixture.[38] A tunable mid-band optical parametric oscillator (OPO) pumped by a Nd:YAG laser (Continuum Horizon II and Surelite EX) generated UV pulses over the wavelength range of 390–210 nm with a linewidth of ~7 cm^{-1}. The time delay between the ionization and photolysis laser pulses was held at ~60 ns. The wavelength-dependent UV pulse energies were continuously monitored with an energy meter and ranged between 1–2 mJ. A stack of velocity-mapping electrodes accelerated ionic photofragments towards a position sensitive detector that comprised a fast-gated microchannel plate/phosphor screen assembly (Photonis) and CCD camera (Basler), while the total phosphorescence was collected with a silicon photomultiplier. Custom-written data acquisition software (National Instruments, LabVIEW) performed real-time centroiding and event-counting.

Images were recorded using conventional velocity-map ion imaging, and analyzed using the polar onion-peeling approach.[39]

Ab initio electronic structure calculations were performed using QChem.[40] All excited state energies were calculated using the ionization potential variant of EOM-CC(2,3) from the restricted Hartree-Fock neutral singlet reference.[41] EOM-CC(2,3) includes single, double, and triple excitations for high-accuracy characterization of excited states. All oscillator strengths were calculated using the excitation energy variant of EOM-CCSD.[42] For all calculations, Dunning's cc-pVTZ basis set was employed.[43] The geometry of neutral acetaldehyde was calculated at the CCSD(T) level of theory.[44,45] All calculations were performed in the frozen core approximation.

Results

Time-of-flight mass spectra recorded with VUV only, UV only, and both VUV+UV pulses present are shown in Figure 2. Single-photon ionization at 118.2 nm yields a mass spectrum dominated by a single intense peak at 6.18 μs that corresponds to the acetaldehyde cation, CH_3CHO^+. Introduction of the UV beam after VUV ionization results in dissociation of CH_3CHO^+, as evidenced by a depletion of the m/z = 44 signal and the appearance of several new features at shorter flight times. The major ionic fragment is HCO^+ at a flight time of 5.06 μs, while additional features in the mass spectrum at 3.68 μs, 3.80 μs, and 6.12 μs are assigned to CH_3^+, CH_4^+, and $C_2H_3O^+$, respectively. The 308 nm UV beam produces a small non-resonant background signal that appears primarily at the parent mass. One-color background signals of similar relative magnitude were observed across the 210–400 nm UV wavelength range.

A well-known problem encountered when working with acetaldehyde expansions is cluster formation.[36,46] Acetaldehyde dimers, trimers, and larger clusters are also observable in the mass spectrum following ionization at 118.2 nm. Ion imaging measurements of CH_3 fragments produced by photolysis of the neutral molecule provide a more discriminating diagnostic; under cluster-free

conditions, the image at 308 nm appears as a clean, isotropic ring at speeds of ~1700 m s^{-1}, while photolysis of clusters results in higher ion counts near the center. Cluster contributions were minimized by operating early in the gas expansion, albeit at the cost of smaller signal magnitudes and likely slightly poorer cooling.

1. Photofragment Yield Spectroscopy

Two-color VUV+UV time-of-flight mass spectra were recorded as the photolysis laser wavelength was scanned over the range 390–210 nm, corresponding to an excitation energy range of 3.18–5.90 eV and converted into the PHOFY spectra shown in Figure 3(a). The excitation energy range is equivalent to 13.41–16.13 eV relative to the ground state of neutral CH_3CHO. PHOFY spectra were obtained by integrating the CH_3^+, CH_4^+, and HCO^+ and $C_2H_3O^+$ peaks in the mass spectra after subtraction of the one-color background signals. The spectra were subsequently normalized to correct for the reproducible wavelength dependence of the photolysis laser fluence. The ~300 ns phosphorescence lifetime of the detector, coupled with the short time delay between the laser pulses resulted in significant overlap of the one-color VUV-only parent ion signal at m/z = 44 and that of the two-color VUV+UV $C_2H_3O^+$ product signal at m/z = 43. Consequently, the $C_2H_3O^+$ yield spectrum is noisier than the others.

CH_3^+ ions are observed only at λ < 317 nm, broadly consistent with the appearance energy (AE) for CH_3^+ of 14.08 eV (or 3.85 eV above the CH_3CHO^+ ground state, implying a threshold wavelength of 322 nm) determined in one-color photoelectron spectroscopy/PEPICO measurements.[32] In contrast, channel I, II, and IV ions have lower AEs (see Table 2) and are observed across the complete range of wavelengths spanned by the PHOFY spectra.[32] Despite the variation among the AEs, the spectra are remarkably similar, with maximum ion yields observed at 249 nm (4.98 eV). The 249 nm feature is most distinct in the CH_3^+ PHOFY spectrum, where it is accompanied by a shoulder at 289 nm (4.29 eV); the other fragment ion yields share these features. Features in the total PHOFY spectra, obtained

by summing over all fragments, appear at wavelengths similar to those observed in photoelectron spectroscopy, as shown in Figure 4, although with very different relative intensities.

The fragment ion yields can be used directly to determine the wavelength-dependent branching fractions shown in Figure 3(b), which is analogous to the breakdown curves presented in the PEPICO studies.[29,30] At $\lambda > 317$ nm, HCO^+ accounts for a fractional yield of ~0.8, with the remainder split equally between $C_2H_3O^+$ and CH_4^+. At $\lambda < 317$ nm the CH_3^+ channel opens and the subsequent increase in its branching fraction is mirrored by a decline in that of HCO^+, which reaches ~0.4 at 210 nm. The branching fractions for the minor CH_4^+ and $C_2H_3O^+$ channels remain effectively constant at ~0.1 across the photolysis wavelength range. The branching fractions are in good agreement with the 2+1 REMPI results of Lee *et al.*,[16] who reported fractional yields of 0.12, 0.73, and 0.15 for $C_2H_3O^+$, HCO^+, and CH_4^+ ions, respectively, at the REMPI wavelength of 363 nm. Averaged over the 346–371 nm range where the branching fractions are wavelength-independent, we find 0.12±0.03, 0.80±0.04, 0.08±0.04 for the same fragment ions (the CH_3^+ yield is zero at $\lambda > 317$ nm). At shorter wavelengths, the observed branching is broadly in agreement with the breakdown curve reported by Johnson *et al.*[30]

2. Ion Imaging

Ion images of CH_3^+, CH_4^+, HCO^+, and $C_2H_3O^+$ photofragments were collected at eleven photolysis wavelengths in the range 316–228 nm, corresponding to excitation energies spanning the range 3.92–5.44 eV (or 14.15–15.67 eV relative the ground state of neutral CH_3CHO). Representative ion images of the four major ionic photofragments resulting from photolysis of CH_3CHO^+ at photolysis wavelengths (316 nm, 276 nm, and 236 nm) are shown in Figure 5. The images are wavelength-dependent to varying degrees and characteristic of each ion; they will be discussed in turn below. Speed and angular distributions were extracted from the ion images using the polar onion-peeling

algorithm.[39] Speed distributions were converted into total translational energy distributions, $P(E_T)$, using the appropriate Jacobian transformation and the equation

$$E_T = \frac{1}{2} m_{ion}(1 + \frac{m_{ion}}{m_{neutral}}) v_{ion}^2$$

where m_{ion} and $m_{neutral}$ are the masses of the observed ion and undetected neutral fragment, respectively. The total E_T distributions are the average of those obtained from at least three independently-measured ion images at each photolysis wavelength. By conservation of energy, E_T is given by

$$E_T = E_{AVL} - E_{INT,fragments} + E_{INT,parent}$$

where the available energy, $E_{AVL} = h\nu - D_0$, is the difference between the photolysis photon energy and the dissociation energy for formation of the detected product ion and corresponding neutral co-fragment.[47] $E_{INT,fragments}$ represents their combined internal energies. The final term, $E_{INT,parent}$, is the internal energy of the parent cation prior to photolysis, which is small due to rotational cooling in the supersonic expansion and the highly vertical ionization step. High-resolution threshold photoelectron spectroscopy measurements[28] show that the parent cations are formed predominantly (71%) in the zero-point level. Around 20% are formed with one quantum of excitation in the ν_7 (CH_3 deformation) mode with the remainder distributed in ν_6 and ν_9 (CH bend and CC stretch vibrational modes, respectively). Consequently, CH_3CHO^+ is formed relatively cold with an average internal energy of $\langle E_{INT,parent} \rangle$ = 350 cm^{-1}. Angular distributions were fit to the usual expression:

$$I(\theta) \propto 1 + \beta_2 P_2(\cos\theta) + \beta_4 P_4(\cos\theta) + \cdots$$

where the β_n are anisotropy parameters and the P_n are Legendre polynomials. No terms beyond second order were significantly different from zero and the angular distributions can be characterized by a single anisotropy parameter, β (= β_2).

Channel I: $C_2H_3O^+ + H$

The lowest energy product channel is H-atom loss, with a dissociation energy D_0 of only 0.528 eV and a minimum AE for m/z = 43 ions of 0.67 eV if the ionic co-fragment is assumed to be acetylium (CH_3CO^+). Several higher energy $C_2H_3O^+$ isomers are also energetically accessible (see Figure 1). The lowest two energy isomers are 1-hydroxyvinylium (CH_2CHO^+) and oxiranylium ($O[CH_2CH]^+$) with energies of 1.296 eV and 2.431 eV relative to acetylium, respectively.[47] However, these isomers cannot be distinguished directly in these measurements. Despite the relatively large values of E_{AVL}, the unfavorable mass ratio between the $C_2H_3O^+$ ion and the H-atom co-fragment restricts the maximum allowed speeds (v_{max} ~590–710 m s^{-1}) and the ion images are small. The representative $C_2H_3O^+$ ion images shown in Figure 5 have been magnified by a factor of two relative to the others to show the ring structure more clearly. At longer wavelengths (λ > 252 nm), a single ring is observed, which increases in radius as the available energy increases. The most probable speeds, however, remain significantly less than v_{max}, indicating internal excitation of $C_2H_3O^+$ as $E_{INT,H}$ is necessarily zero. A second, smaller ring is evident at λ ≤ 252 nm (see the 236 nm ion image in Figure 5) and three rings can be distinguished at the shortest photolysis wavelength of 228 nm. The $C_2H_3O^+$ angular distributions are isotropic at all photolysis wavelengths, in contrast to the one-color REMPI study of Lee *et al*., where anisotropy parameters up to β_6 were non-zero.[16]

The E_T distributions are decomposed by fitting to one, two, or three Gaussian functions. Each component can be characterized by the average translational energy, $\langle E_T \rangle$, and the standard deviation, σ_{E_T}. The latter parameter is characteristic of each component and insensitive to photolysis wavelength. The fastest component is present at all λ, has an approximately constant $\langle E_T \rangle$ of ~1.1 eV between 316 nm and 284 nm, beyond which it increases linearly with E_{AVL}, reaching 2.24 eV. It also has the largest $P(E_T)$ spread, with σ_{E_T} = 0.83±0.08 eV. The distributions become clearly bimodal at λ ≤ 252 nm and the second, slower component has $\langle E_T \rangle$ values that increase linearly with E_{AVL} over the

range 0.73–2.24 eV. It is also narrower, with σ_{E_T} = 0.52±0.03 eV. The third and slowest component, which is observed only at the shortest photolysis wavelength of 228 nm, has $\langle E_T \rangle$ = 0.65 eV and σ_{E_T} = 0.37 eV. In contrast to the other product channels discussed below, for which the undetected neutral fragment has internal degrees of freedom, the E_T distributions for the H-atom loss channel can be converted unambiguously into $C_2H_3O^+$ internal energy distributions using $E_{INT} = E_{AVL} - E_T$. The $C_2H_3O^+$ E_{INT} distributions obtained at 316 nm, 276 nm, and 236 nm are shown in Figure 6. The conversion from E_T to E_{INT} assumes production of the lowest energy $C_2H_3O^+$ isomer, acetylium, CH_3CO^+; the relative energies of other higher-energy $C_2H_3O^+$ isomers are also indicated. Values of E_{INT} > 3.30 eV are sufficient for CH_3CO^+ to undergo secondary dissociation to CH_3^+ + CO. As can be seen in Figure 6, the $P(E_{INT})$ distributions extend slightly beyond this value at 276nm, while the secondary component in the 236 nm data lies entirely beyond this threshold.

Channel II: $HCO^+ + CH_3$

The major fragmentation channel producing formyl cations and neutral methyl radicals is the second lowest energy pathway, with D_0 = 1.510 eV and AE = 1.80 eV. E_{AVL} ranges from 2.41–3.93 eV. Representative ion images are shown in Figure 5. The maximum ion count density occurs near the image centers and declines to zero at speeds around half of v_{max} (2.34–2.99 km s^{-1}), indicating preferential partitioning of E_{AVL} into internal degrees of freedom of the HCO^+ and CH_3 fragments. The corresponding E_T distributions, shown in Figure 7(a), peak near zero with modest $\langle E_T \rangle$ values of 0.24–0.34 eV. The fraction of the available energy partitioned into translation, f_T, increases linearly with E_{AVL} from 0.06 to 0.14. The images are anisotropic at all wavelengths, with similar E_T-dependent anisotropy parameters, $\beta(E_T)$, that increase near-linearly from zero to +0.8 at the maximum observed E_T of ~1 eV, as shown in Figure 7(b). Lee *et al*. have obtained similarly anisotropic images, in one-color measurements at 363 nm that used REMPI to prepare the parent cation.[16]

Channel III: CH_3^+ + HCO

The thermodynamic threshold for formation of CH_3^+ + HCO is 3.20 eV, limiting E_{AVL} to the range 0.72–2.24 eV. CH_3^+ ion images (representative examples are shown in Figure 5) are isotropic and dominated by large ion counts near the center. The radial distributions are curtailed at speeds significantly lower than v_{max} (2.47–4.35 km s^{-1}) and increase only slightly as the photolysis wavelength is decreased. The E_T distributions shown in Figure 8(a) peak at zero and drop off rapidly, appearing characteristic of statistical unimolecular dissociation on a surface without a barrier. As E_{AVL} increases, the distributions broaden slightly and the small values of $\langle E_T \rangle$ vary over the range 0.06–0.16 eV. The fraction of E_{AVL} partitioned into translation is independent of photolysis wavelength, with an average value of f_T = 0.068±0.008.

Channel IV: CH_4^+ + CO

The dissociation energy for channel IV is D_0 = 2.13 eV and E_{AVL} spans the range 1.80–3.31 eV. Ion images of CH_4^+ fragments have isotropic features at the image centers that are similar to those observed for CH_3^+ but are accompanied by a faster, anisotropic component that is distinct at photolysis wavelengths λ ≤ 300 nm, as shown in Figure 5. The most probable speeds of the fast component increase with excitation energy from 1.5 km s^{-1} to 3.0 km s^{-1}, but these speeds are still significantly smaller than the v_{max} determined by conservation of energy and momentum which span the range 3.7–5.0 km s^{-1}. The E_T distributions in Figure 9(a) clearly show the two components at shorter wavelengths. The slow components peak near zero at all wavelengths, and like CH_3^+, appear to indicate statistical barrierless dissociation. The slow and fast E_T components can be distinguished at λ ≤ 300 nm by fits using Gumbel and Gaussian functions, respectively. $\langle E_T \rangle$ values for the anisotropic fast component increase from 0.40 eV at 300 nm to 1.20 eV at 228 nm; f_T also increases from 0.20 to 0.36. The spread in the fast component, which is characterized by the standard deviation of the Gaussian fit, increases from 0.18 eV at 300 nm before reaching a plateau at ~0.3 eV at λ ≤ 268

nm. The fast component is anisotropic, with maximum intensity found at the poles, parallel to the laser polarization axis. At shorter wavelengths, where the two components are distinct, the anisotropy parameter for the fast component reaches a value of $\beta \approx +1$, indicating that CH_4^+ is formed promptly with recoil velocities that are preferentially parallel to the polarization of the UV photolysis laser. Smaller values of β at longer wavelengths are due to significant overlap with the isotropic slow component.

Discussion

Figure 4 shows the total photofragment ion yield spectrum, summed over all detected fragments, alongside the photoelectron spectrum measured by Cvitaš *et al.*[28] Ionization energy EOM-CC(2,3)/cc-pVTZ calculations reliably predict the energies of the bands observed in the photoelectron spectrum. The dominant feature in the PHOFY spectrum coincides approximately with the C̃ band in the photoelectron spectroscopy measurements at an excitation energy of approximately 4.9 eV (~250 nm in the PHOFY spectra shown in Figure 3) above the ground state of the CH_3CHO^+ cation. It is accompanied by a shoulder at 4.3 eV (~290 nm), and a tail that extends beyond the range of the measurements. Also shown in Figure 4 are the vertical excitation energies and corresponding oscillator strengths from EOM-CC/cc-pVTZ calculations. The first excited state $\tilde{A}^2A''$ has a vertical excitation energy of 3.08 eV and an oscillator strength of only 6.5×10^{-5}. The $\tilde{B}^2A'$ state at 4.24 eV has a slightly greater oscillator strength of 2.1×10^{-4} while that of the $\tilde{C}^2A'$ state at 5.03 eV is significantly larger at 1.6×10^{-2}. Consequently, the dominant feature in the PHOFY spectrum is assigned to a transition to the $\tilde{C}^2A'$ state while the weaker shoulder and signal observed to longer wavelengths are due to excitation to the $\tilde{B}^2A'$ and A^2A'' states. It seems likely that the excitation wavelength range used for the ion imaging measurements (316–228 nm) primarily accesses the $\tilde{C}^2A'$ state of CH_3CHO^+.

The differences in the photofragment yield and photoelectron spectra shown in Figure 4 can be readily justified. The photoelectron spectroscopy and PEPICO measurements used thermal samples

of acetaldehyde and involve single photon ionization, with subsequent fragmentation. Consequently, the observed fragment yields represent the product of the VUV photoionization cross-section with the fragmentation quantum yields. In contrast, VUV ionization near threshold first produces internally cold ions, which are subsequently fragmented by the UV pulse to yield the PHOFY spectra. That is, in the current measurements, the wavelength-dependent photofragment yields represent the equivalent fragmentation quantum yields, but now modified by the absorption cross sections for spectroscopic transitions of the ion.

The observation of CH_3^+ signal onset at $\lambda \approx 317$ nm (3.91 eV) implies an AE of 14.12 eV, a value that is in excellent agreement with previous PIMS and PEPICO measurements.[29,30,32] As has been commented on previously,[30,32] the CH_3^+ AE coincides closely with the adiabatic excitation energy required to access the B^2A' state, which is 0.71 eV higher than the thermodynamic threshold. However, the total translational energy distributions observed for CH_3^+ peak very close to zero and appear to be consistent with statistical and barrierless unimolecular dissociation on the $\tilde{X}^2A'$ surface following internal conversion. It seems likely that the increase in CH_3^+ yield at $\lambda < 317$ nm is due to the increase in the absorption cross section coincident with the energy threshold being reached, rather than dissociation occurring specifically on the $\tilde{B}^2A'$ surface or, as is more likely, the $\tilde{C}^2A'$ surface. As the CH_3^+ E_T distributions appear statistical, we model them using phase space theory (PST).[48,49] The PST calculations use theoretical spectroscopic constants calculated at the MP2/aug-cc-pVTZ level;[50] CH_3^+ is treated as an oblate symmetric top and HCO as a near-prolate symmetric top. The normalized E_T distributions calculated using PST are shown alongside the experimental measurements in Figure 8 for a subset of the photolysis wavelengths used. In general, the experimental E_T distributions are close to statistical. The deviation from statistical behavior can be characterized using a linear surprisal analysis, in which the surprisal is evaluated as a function of the translational energy

$$I(E_T) = -\ln[P(E_T)/P^\circ(E_T)] = a + bE_T$$

where $P(E_T)$ is the experimental distribution and $P°(E_T)$ is the statistical prior distribution, here obtained from the PST calculations. Figure 8 shows plots of the surprisal as a function of the translational energy. The plots are linear, with positive gradients ($b > 0$) indicating that the experimental distributions are somewhat colder than statistical. The gradients initially decrease monotonically as the available energy increases, meaning the experimental distributions become increasingly statistical, before reaching a constant value of ~1 at photolysis wavelengths less than 260 nm.

CH_3^+ E_T distributions that are colder than statistical are consistent with some fraction being formed by secondary dissociation of internally excited CH_3CO^+ formed by the H-atom loss pathway:

$$CH_3CHO^+ \rightarrow CH_3CO^+ + H \rightarrow CH_3^+ + CO + H \qquad III'$$

The triple fragmentation channel III′ can occur for CH_3CO^+ primary fragments with $E_{INT} > 3.30$ eV; that is, it is energetically accessible at all wavelengths used in the ion imaging experiments. Kable and co-workers have modelled triple fragmentation in the photochemistry of neutral acetaldehyde using sequential applications of PST to model the primary and secondary dissociation steps.[51] E_T distributions arising from triple fragmentation pathways are universally colder than the statistical distributions obtained for a two-body fragmentation pathway leading to the same products. Johnson *et al*. measured $\langle E_T \rangle$ values for CH_3CO^+ fragments over a range of excess energies in PEPICO experiments and found a marked increase in the gradient above 3.6 eV (equivalent to a photolysis wavelengths of $\lambda < 344$ nm).[30] The observed increase in $\langle E_T \rangle$ was attributed to loss of the low-E_T (high-E_{INT}) component due to secondary dissociation. A similar increase in $\langle E_T \rangle$ values for $C_2H_3O^+$ is observed obtained in the current work (discussed in more detail below) at $E_{AVL} > 3.8$ eV, which is entirely consistent with the threshold for triple fragmentation via channel III′.

Triple fragmentation pathways are strongly entropically favored and tend to become increasingly dominant as the available energy is increased beyond the threshold.[51] However, the CH_3^+ surprisal

analysis suggests the opposite trend. Namely, the experimental E_T distributions for channel III deviate most from the two-body fragmentation PST distributions at low excitation energies and become increasingly statistical as E_{AVL} increases. This observation suggests that the triple fragmentation channel III′ contributes most to the observed E_T distributions at the longest photolysis wavelengths, becoming less important at shorter wavelengths. The inflexion point in the plot of the surprisal parameter b against wavelength at $\lambda \leq 260$ nm (E_{AVL} = 4.24 eV) shown in Figure 8(c) coincides with the clear onset of bimodality in the $C_2H_3O^+$ E_{INT} distributions. While this may be coincidental, it will be argued below that the low-E_T components are due to H-atom loss from higher-energy CH_3CHO^+ isomers. As none of the other possible $C_2H_3O^+$ isomers can readily dissociate to form CH_3^+, we suggest that isomerization becomes increasingly competitive with dissociation to form CH_3CO^+ + H and consequently the three-body fragmentation channel III′ is attenuated.

Barriers of 2.9–3.1 eV have been identified for keto-enol tautomerization $CH_3CHO^+ \rightarrow CH_2CHOH^+$ on the lowest cationic surface.[52,53] Tautomerization is therefore possible at all excitation wavelengths. As shown in Figure 6, the $C_2H_3O^+$ E_{INT} distribution is unimodal at photolysis wavelengths $\lambda > 260$ nm. The small E_T release is consistent with dissociation over a small barrier, most probably on the ground state following internal conversion, leading to CH_3CO^+ + H. Most of the available energy is partitioned into internal degrees of freedom of the cation fragment and even at the longest excitation wavelength, E_{AVL} is sufficient for secondary dissociation to CH_3^+ + CO (channel III′). As E_{AVL} increases, the E_{INT} distribution increasingly extends beyond the dissociation threshold for channel III′, becoming clearly bimodal at $\lambda \leq 260$ nm ($E_{AVL} \geq 4.24$ eV). $C_2H_3O^+$ fragments with $E_{INT} > 3.30$ eV are attributed to fragment isomers other than CH_3CO^+ that are formed by H-atom loss following parent isomerization. Figure 6 shows the energies of the two lowest-lying isomers of acetaldehyde cation, vinyl alcohol and oxirane cations. H-atom loss from these species is expected to form primarily 1-hydroxyvinylium and/or oxiranylium cations, with a high degree of internal excitation but insufficient energy to undergo secondary dissociation. We assign the features in the E_{INT} distributions energy order – the

secondary component evident at λ ≤ 260 nm is attributed to $C_2H_3O^+$ fragments resulting from H-atom loss from vinyl alcohol cation and the tertiary component that is observed at 228 nm is attributed to H-atom loss from oxirane cation. Isomerization appears to become increasingly competitive with CH_3CHO^+ dissociation as E_{AVL} increases, leading to a concomitant reduction in the amount of secondary dissociation of CH_3CO^+ and hence the variation in the linear surprisal parameter with photolysis wavelength.

Another possible origin for the low-E_T components is formation of electronically excited CH_3CO^+. However, the lowest lying triplet and singlet states of CH_3CO^+ lie at 5.18 and 6.17 eV (239 and 201 nm) above the parent cation ground state, respectively.[54] We conclude that the appearance of the second feature at λ ≤ 260 nm is not consistent with formation of electronically excited CH_3CO^+.

The fragmentation dynamics observed for channel IV are particularly intriguing. First, we note that CH_4^+ is observed at all excitation wavelengths. In contrast, Johnson *et al*.[30] were unable to observe CH_4^+ once the excitation energy was sufficient to excite on the $\tilde{B}$ band and they attributed CH_4^+ production specifically to photochemistry of the $\tilde{A}^2A''$ state. The presence of two distinct components in the E_T distributions at short wavelengths, seen in Figure 9(a), indicates formation of CH_4^+ *via* two pathways. The translationally fast component is anisotropic, with $\beta \approx +1$ at 236 nm while the slow component that peaks near zero is isotropic. Extrapolating from shorter wavelengths suggests that these two features are heavily overlapped at λ > 292 nm and the E_T-averaged anisotropy of $\langle\beta\rangle \approx +0.3$ at 316 nm is consistent with contributions from both components. The values for the anisotropy parameter are in reasonable agreement with observations made by Lee *et al.*[16] who reported β = 0.5±0.1 for CH_4^+ at 363 nm, where the fast and slow components are unresolved. The anisotropy of the fast component is clearly inconsistent with excitation to the $\tilde{A}^2A''$ state.

The isotropic slow component appears to be consistent with a largely statistical dissociation on the ground state surface with little or no barrier.[55] The E_T distributions were modeled using PST as

previously using both calculated and experimental spectroscopic data.[50,56] The normalized PST distributions are shown alongside experimental data in Figure 9(b). In general, the experimental E_T distributions appear close to statistical, but a linear surprisal analysis produces a wavelength independent surprisal parameter with an average value of $\langle b \rangle$ = 2.4±0.1. A positive surprisal parameter again indicates that the experimental E_T distributions are colder than statistical, as was the case for CH_3^+. While the colder-than-statistical E_T distributions for CH_3^+ were attributed to contributions from secondary dissociation of internally excited CH_3CO^+ formed in channel I, there are no simple (and barrierless) bond cleavage pathways that lead to the molecular cation CH_4^+. As in neutral acetaldehyde, a significant barrier might be expected for decomposition to form molecular products on the ground state, and consequently more substantial release of the available energy as translation. One possible explanation for low E_T fragments with high internal energy that has been suggested by Lee *et al.*[16] for CH_4^+ production is roaming. Highly internally excited CH_4 is produced by roaming mechanisms involving intramolecular reaction of nascent radical products CH_3 + HCO in the photodissociation of neutral acetaldehyde.[57] In the photochemistry of the acetaldehyde cation, however, either 'radical' may carry the charge and two intramolecular reactions could plausibly lead to formation of CH_4^+ + CO. One is long range proton transfer between CH_3 + HCO^+ and the second is H-atom abstraction reaction CH_3^+ + HCO. The current experiments cannot distinguish between these possibilities, and we acknowledge that a roaming mechanism is highly speculative. Improved characterization of the fragment internal energy distributions or, better, correlated product state measurements and theoretical support are essential.

The effect of roaming dynamics in the photochemistry of ions is an interesting question that has been little explored to date. Roaming in ion-molecule reactions has been discussed recently by Mauguière et al.[58–60] from the perspective of a phase space interpretation of the dynamics. An example of roaming, albeit before the term roaming was coined, in an ionic system highlighted by Mauguière et al.[58] (and earlier by Klippenstein et al.[61]) is the decomposition of metastable protonated propylamine

to form propyl radicals and ammonium cations studied by Audier and Morton.[62] It is quite possible that the presence of long-range attractive ion-dipole or ion-induced dipole interactions between the charged and neutral 'radical' products means roaming may be a general phenomenon in the fragmentation of ionic species.

The observation of anisotropic angular distributions for the translationally fast CH_4^+ fragments implies prompt dissociation, which is surprising for the molecular fragment. The positive anisotropy parameter is consistent with initial excitation being predominantly to the $\tilde{C}^2A'$ (or $\tilde{B}^2A'$) state. The modest translational energy release also indicates that the separating fragments experience some degree of repulsion during the dissociation, which most probably involves passage over a barrier. In neutral acetaldehyde, a high barrier on the S_0 surface can lead to the molecular products CH_4 + CO. A similar, albeit smaller, barrier on the cation $\tilde{X}^2A'$ (or D_0) surface would account for the translational energy release. However, the observed anisotropy requires that the transition state be reached in less than a rotational period. One possibility is that internal conversion occurs *via* a conical intersection between the $\tilde{B}^2A'$ or $\tilde{C}^2A'$ surfaces and the $\tilde{X}^2A'$ surface that is close to the molecular transition state in configuration space. After internal conversion, the system is able to dissociate promptly. *Ab initio* calculations characterizing these regions of the cation potential energy surface are highly desirable. Formation of electronically excited CH_4^+ is possible, with the $\tilde{A}$ state lying only 0.41 eV above the CH_4^+ ground state.[63] The electronic energy is a small fraction of E_{AVL} for channel IV, however, and would result into only a marginal decrease in f_T if the $\tilde{A}$ state were formed. The current measurements are unable to distinguish between ground and excited state CH_4^+.

Finally, the experimental E_T distributions for the most abundant fragment HCO^+ shown in Figure 7(a) peak near zero and agree with the results of the PEPICO measurements of Johnson *et al.*,[30] and the ion imaging study by Lee *et al.*[16] While this appears to be broadly consistent with a statistical unimolecular dissociation mechanism, two pieces of experimental evidence suggest that this is not the complete story. First, the ion images shown in Figure 5 are clearly anisotropic, which is indicative

of prompt, i.e. non-statistical, dissociation. Second, the anisotropy is highly E_T-dependent, increasing from zero to ~+1 as shown in Figure 7(b), which suggests that there may be two unresolved components in the E_T distributions. The presence of two components is supported by a linear surprisal analysis, shown in Figure 7(c). PST distributions calculated using both calculated and experimental spectroscopic constants taken from the literature[50,51] clearly do not reproduce the experimental data. The surprisal however clearly contains two linear components; the gradient is zero at low E_T and non-zero at higher E_T. We conclude that the observed E_T distributions for HCO^+ contain two unresolved components, one isotropic and statistical and the other anisotropic, with modest portioning of E_{AVL} into translation. The relative contribution of each component is E_T-dependent and pulls the value of β to higher or lower values. The HCO^+ observations therefore appear to be very similar to those observed at longer photolysis wavelengths for CH_4^+, with the only major difference being that the 'fast' anisotropic component for the former remains heavily overlapped with the slow statistical components. The statistical component is likely formed by dissociation on the $\tilde{X}^2A'$ surface following internal conversion as suggested by previous studies.[29,30] The provenance of the anisotropic component is more difficult to discern. While the positive anisotropy is consistent with a prompt dissociation following excitation to the $\tilde{B}^2A'$ and the $\tilde{C}^2A'$ states, a remarkably small fraction of the available energy is partitioned into translation.

Direct fragmentation of polyatomic cations on electronically excited states is a relatively unusual occurrence. In mass spectrometric applications, ion fragmentation is often assumed to proceed statistically as described by the quasi-equilibrium theory (QET), in which dissociation depends only on total energy rather than the nature of the excitation.[25,26] Excited state dynamics in polyatomic cations was recently observed by Gichuhi *et al.*,[19] who used velocity map imaging to detect $HCNH^+$ fragments formed after excitation of ethylamine cations ($CH_3CH_2NH_2^+$) at 233 nm. Two components were also observed in the E_T distributions: a dominant slow component peaking at $E_T \approx 0$ and a minor

fast component. The anisotropy parameter β also increased linearly with photofragment speed, as observed in our measurements of CH_4^+ and HCO^+.

Conclusion

Velocity-map ion imaging and photofragment yield spectroscopy have been used to study the photofragmentation dynamics of internally cold CH_3CHO^+ cations, produced in a molecular beam by single-photon VUV ionization at 118 nm. The total fragment ion yield reaches a maximum at ~250 nm, corresponding to excitation to the $\tilde{C}^2A'$ state. A weaker shoulder attributed to the $\tilde{B}^2A'$ state is observed at ~290 nm. At $\lambda > 317$ nm, fragmentation via channel II to form $HCO^+ + CH_3$ dominates; at $\lambda < 317$ nm channel III forming $CH_3^+ + HCO$ opens and the fractional yield of channel II decreases. Ion imaging measurements detecting $C_2H_3O^+$, HCO^+, CH_3^+ and CH_4^+ show fragment-specific and wavelength-dependent dissociation mechanisms. The photochemistry and fragmentation dynamics of polyatomic ions appears to be particularly rich, involving isomerization, statistical and dynamical dissociation, and multiple pathways to products. State-specific detection of fragments would provide useful additional experimental data to obtain further insights but are likely to be confounded by neutral dissociation products; complementary theoretical work to better characterize the ionic potential energy surfaces will be essential.

Acknowledgements

This material is based upon work supported by the National Science Foundation under Grant No. CHE-1566064. Acknowledgment is made to the Donors of the American Chemical Society Petroleum Research Fund for partial support of this research. L.M.M. would like to thank the Zuckerman STEM Leadership Program for support.

References

1 T. J. Millar, Astrochemistry, *Plasma Sources Sci. Technol.*, 2015, **24**, 043001.

2 S. Petrie and D. K. Bohme, Ions in space, *Mass Spectrom. Rev.*, 2007, **26**, 258–280.

3 R. C. Henry, The Local Interstellar Ultraviolet Radiation Field, *Astrophys. J.*, 2002, **570**, 697–707.

4 G. A. Blake, C. R. Masson, T. G. Phillips and E. C. Sutton, The rotational emission-line spectrum of Orion A between 247 and 263 GHz, *Astrophys. J. Suppl. Ser.*, 1986, **60**, 357.

5 S. Cazaux, A. G. G. M. Tielens, C. Ceccarelli, A. Castets, V. Wakelam, E. Caux, B. Parise and D. Teyssier, The Hot Core around the Low-Mass Protostar IRAS 16293-2422: Scoundrels Rule!, *Astrophys. J.*, 2003, **593**, L51–L55.

6 A. A. Jaber, C. Ceccarelli, C. Kahane and E. Caux, The Census of Complex Organic Molecules in the Solar-type Protostar IRAS16293-2422, *Astrophys. J.*, 2014, **791**, 29-.

7 M. A. Requena-Torres, J. Martín-Pintado, A. Rodríguez-Franco, S. Martín, N. J. Rodríguez-Fernández and P. de Vicente, Organic molecules in the Galactic center: Hot core chemistry without hot cores, *Astron. Astrophys.*, 2006, **455**, 971–985.

8 B. E. Turner, R. Terzieva and E. Herbst, The Physics and Chemistry of Small Translucent Molecular Clouds. XII. More Complex Species Explainable by Gas-Phase Processes, *Astrophys. J.*, 1999, **518**, 699–732.

9 J. Crovisier, D. Bockelée-Morvan, P. Colom, N. Biver, D. Despois and D. C. Lis, The composition of ices in comet C/1995 O1 (Hale-Bopp) from radio spectroscopy, *Astron. Astrophys.*, 2004, **418**, 1141–1157.

10 O. P. J. Vieuxmaire, M. G. D. Nix, J. A. J. Fitzpatrick, M. Beckert, R. N. Dixon and M. N. R. Ashfold, Predissociation of state selected Br_2^+ cations, *Phys. Chem. Chem. Phys.*, 2004, **6**, 543–554.

11 O. P. J. Vieuxmaire, N. H. Nahler, J. R. Jones, R. N. Dixon and M. N. R. Ashfold, Photodissociation of state selected $BrCl^+$ cations: branching ratios and angular anisotropies of the Br^+ product forming channels, *Mol. Phys.*, 2005, **103**, 2437–2452.

12 O. P. J. Vieuxmaire, N. H. Nahler, R. N. Dixon and M. N. R. Ashfold, Multiphoton dissociation dynamics of BrCl and the $BrCl^+$ cation, *Phys. Chem. Chem. Phys.*, 2007, **9**, 5531–5541.

13 S. H. Gardiner, T. N. V. Karsili, M. L. Lipciuc, E. Wilman, M. N. R. Ashfold and C. Vallance, Fragmentation dynamics of the ethyl bromide and ethyl iodide cations: a velocity-map imaging study, *Phys. Chem. Chem. Phys.*, 2014, **16**, 2167–2178.

14 A. D. Webb, N. H. Nahler and M. N. R. Ashfold, Imaging Studies of the Photodissociation of NH_3^+ and ND_3^+ Cations, *J. Phys. Chem. A*, 2009, **113**, 3773–3778.

15 A. G. Sage, T. A. A. Oliver, R. N. Dixon and M. N. R. Ashfold, Velocity map imaging studies of the photodissociation of H_2O^+ cations, *Mol. Phys.*, 2010, **108**, 945–955.

16 S. K. Lee, R. Silva, M. H. Kim, L. Shen and A. G. Suits, Photodissociation of Spatially Aligned Acetaldehyde Cations, *J. Phys. Chem. A*, 2007, **111**, 6741–6745.

17 M. H. Kim, L. Shen, H. Tao, T. J. Martinez and A. G. Suits, Conformationally Controlled Chemistry: Excited-State Dynamics Dictate Ground-State Reaction, *Science*, 2007, **315**, 1561–1565.

18 L. Shen, P. C. Singh, M. Kim, B. Zhang and A. G. Suits, Ion and Electron Imaging Study of Isobutanal Photoionization Dynamics, *J. Phys. Chem. A*, 2009, **113**, 68–74.

19 W. K. Gichuhi, A. M. Mebel and A. G. Suits, UV Photodissociation of Ethylamine Cation: A Combined Experimental and Theoretical Investigation, *J. Phys. Chem. A*, 2010, **114**, 13296–13302.

20 P. C. Singh, L. Shen, J. Zhou, H. B. Schlegel and A. G. Suits, Photodissociation Dynamics of Methylamine Cation and Its Relevance to Titan's Ionosphere, *Astrophys. J.*, 2010, **710**, 112.

21 M. H. Kim, B. D. Leskiw and A. G. Suits, Vibrationally Mediated Photodissociation of Ethylene Cation by Reflectron Multimass Velocity Map Imaging, *J. Phys. Chem. A*, 2005, **109**, 7839–7842.

22 M. H. Kim, B. D. Leskiw, L. Shen and A. G. Suits, Vibrationally Mediated Photodissociation of $C_2H_4S^+$, *J. Phys. Chem. A*, 2007, **111**, 7472–7480.

23 P. C. Singh, L. Shen, M. H. Kim and A. G. Suits, Photodissociation and photoelectron imaging of molecular ions: probing multisurface and multichannel dynamics, *Chem. Sci.*, 2010, **1**, 552–560.

24 W. M. Jackson and D. Xu, Photodissociation of the acetone cation at 355 nm using the velocity imaging technique, *J. Chem. Phys.*, 2000, **113**, 3651–3657.

25 J. . Lorquet, Landmarks in the theory of mass spectra, *Int. J. Mass Spectrom.*, 2000, **200**, 43–56.

26 C. Lifshitz, Intramolecular energy redistribution in polyatomic ions, *J. Phys. Chem.*, 1983, **87**, 2304–2313.

27 D. Chadwick and A. Katrib, Photoelectron spectra of acetaldehyde and acetyl halides, *J. Electron Spectrosc. Relat. Phenom.*, 1974, **3**, 39–52.

28 T. Cvitaš, H. Güsten and L. Klasinc, Deuterium shifts in the high resolution photoelectron spectra of acetaldehyde, *J. Chem. Phys.*, 1976, **64**, 2549–2551.

29 R. Bombach, J.-P. Stadelmann and J. Vogt, The fragmentation and isomerization of internal energy selected acetaldehyde molecular cations, *Chem. Phys.*, 1981, **60**, 293–299.

30 K. Johnson, I. Powis and C. J. Danby, A photoelectron—photoion coincidence study of acetaldehyde and ethylene oxide molecular ions, *Chem. Phys.*, 1982, **70**, 329–343.

31 A. J. Yencha, M. R. F. Siggel-King, G. C. King, A. E. R. Malins and M. Eypper, Threshold photoelectron spectroscopy of acetaldehyde and acrolein, *J. Electron Spectrosc. Relat. Phenom.*, 2013, **187**, 65–71.

32 H. W. Jochims, W. Lohr and H. Baumgärtel, Photoionization mass spectrometry studies of deuterated acetaldehydes CH_3CDO and CD_3CHO, *Chem. Phys. Lett.*, 1978, **54**, 594–596.

33 G. J. Fisanick, T. S. E. Iv, B. A. Heath and M. B. Robin, Multiphoton ionization mass spectroscopy of acetaldehyde, *J. Chem. Phys.*, 1980, **72**, 5571–5580.

34 T. S. Eichelberger IV and G. J. Fisanick, Multiphoton ionization spectroscopy of the 3s Rydberg state in the deuterated acetaldehydes, *J. Chem. Phys.*, 1981, **74**, 5962–5970.

35 S. K. Shin, B. Kim, J. G. Haldeman and S.-J. Han, State-Selected Photodissociation of Acetaldehyde Molecular Ion: Hydrogen Scrambling and the Product Branching Ratio, *J. Phys. Chem.*, 1996, **100**, 8280–8284.

36 B. W. Toulson, K. M. Kapnas, D. A. Fishman and C. Murray, Competing pathways in the near-UV photochemistry of acetaldehyde, *Phys. Chem. Chem. Phys.*, 2017, **19**, 14276–14288.

37 B. W. Toulson, D. A. Fishman and C. Murray, Photodissociation dynamics of acetone studied by time-resolved ion imaging and photofragment excitation spectroscopy, *Phys. Chem. Chem. Phys.*, 2018, **20**, 2457–2469.

38 A. H. Kung, J. F. Young and S. E. Harris, Generation of 1182-Å radiation in phase-matched mixtures of inert gases, *Appl. Phys. Lett.*, 1973, **22**, 301–302.

39 G. M. Roberts, J. L. Nixon, J. Lecointre, E. Wrede and J. R. R. Verlet, Toward real-time charged-particle image reconstruction using polar onion-peeling, *Rev. Sci. Instrum.*, 2009, **80**, 053104.

40 Y. Shao, Z. Gan, E. Epifanovsky, A. T. B. Gilbert, M. Wormit, J. Kussmann, A. W. Lange, A. Behn, J. Deng, X. Feng, D. Ghosh, M. Goldey, P. R. Horn, L. D. Jacobson, I. Kaliman, R. Z. Khaliullin, T. Kuś, A. Landau, J. Liu, E. I. Proynov, Y. M. Rhee, R. M. Richard, M. A. Rohrdanz, R. P. Steele, E. J. Sundstrom, H. L. W. III, P. M. Zimmerman, D. Zuev, B. Albrecht, E. Alguire, B. Austin, G. J. O. Beran, Y. A. Bernard, E. Berquist, K. Brandhorst, K. B. Bravaya, S. T. Brown, D. Casanova, C.-M. Chang, Y. Chen, S. H. Chien, K. D. Closser, D. L. Crittenden, M. Diedenhofen, R. A. D. Jr, H. Do, A. D. Dutoi, R. G. Edgar, S. Fatehi, L. Fusti-Molnar, A. Ghysels, A. Golubeva-Zadorozhnaya, J. Gomes, M. W. D. Hanson-Heine, P. H. P. Harbach, A. W. Hauser, E. G. Hohenstein, Z. C. Holden, T.-C. Jagau, H. Ji, B. Kaduk, K. Khistyaev, J. Kim, J. Kim, R. A. King, P. Klunzinger, D. Kosenkov, T. Kowalczyk, C. M. Krauter, K. U. Lao, A. D. Laurent, K. V. Lawler, S. V. Levchenko, C. Y. Lin, F. Liu, E. Livshits, R. C. Lochan, A. Luenser, P. Manohar, S. F. Manzer, S.-P. Mao, N. Mardirossian, A. V. Marenich, S. A. Maurer, N. J. Mayhall, E. Neuscamman, C. M. Oana, R. Olivares-Amaya, D. P. O'Neill, J. A. Parkhill, T. M. Perrine, R. Peverati, A. Prociuk, D. R. Rehn, E. Rosta, N. J. Russ, S. M. Sharada, S. Sharma, D. W. Small, A. Sodt, T. Stein, D. Stück, Y.-C. Su, A. J. W. Thom, T. Tsuchimochi, V. Vanovschi, L. Vogt, O. Vydrov, T. Wang, M. A. Watson, J. Wenzel, A. White, C. F. Williams, J. Yang, S. Yeganeh, S. R. Yost, Z.-Q. You, I. Y. Zhang, X. Zhang, Y. Zhao, B. R. Brooks, G. K. L. Chan, D. M. Chipman, C. J. Cramer, W. A. G. III, M. S. Gordon, W. J. Hehre, A. Klamt, H. F. S. III, M. W. Schmidt, C. D. Sherrill, D. G. Truhlar, A. Warshel, X. Xu, A. Aspuru-Guzik, R. Baer, A. T. Bell, N. A. Besley, J.-D. Chai, A. Dreuw, B. D. Dunietz, T. R. Furlani, S. R. Gwaltney, C.-P. Hsu, Y. Jung, J. Kong, D. S. Lambrecht, W. Liang, C. Ochsenfeld, V. A. Rassolov, L. V. Slipchenko, J. E. Subotnik, T. V. Voorhis, J. M. Herbert, A. I. Krylov, P. M. W. Gill and M. Head-Gordon, Advances in molecular quantum chemistry contained in the Q-Chem 4 program package, *Mol. Phys.*, 2015, **113**, 184–215.

41 S. Hirata, M. Nooijen and R. J. Bartlett, High-order determinantal equation-of-motion coupled-cluster calculations for ionized and electron-attached states, *Chem. Phys. Lett.*, 2000, **328**, 459–468.

42 J. F. Stanton and R. J. Bartlett, The equation of motion coupled-cluster method. A systematic biorthogonal approach to molecular excitation energies, transition probabilities, and excited state properties, *J. Chem. Phys.*, 1993, **98**, 7029.

43 T. H. Dunning Jr., Gaussian basis sets for use in correlated molecular calculations. I. The atoms boron through neon and hydrogen, *J. Chem. Phys.*, 1989, **90**, 1007–1023.

44 K. Raghavachari, G. W. Trucks, J. A. Pople and M. Head-Gordon, A fifth-order perturbation comparison of electron correlation theories, *Chem. Phys. Lett.*, 1989, **157**, 479–483.

45 R. J. Bartlett, J. D. Watts, S. A. Kucharski and J. Noga, Non-iterative fifth-order triple and quadruple excitation energy corrections in correlated methods, *Chem. Phys. Lett.*, 1990, **165**, 513–522.

46 K. L. K. Lee, M. S. Quinn, A. T. Maccarone, K. Nauta, P. L. Houston, S. A. Reid, M. J. T. Jordan and S. H. Kable, Two roaming pathways in the photolysis of CH_3CHO between 328 and 308 nm, *Chem. Sci.*, 2014, **5**, 4633–4638.

47 B. Ruscic, Active Thermochemical Tables (ATcT) values based on ver. 1.122 of the Thermochemical Network; available at ATcT.anl.gov.

48 P. Pechukas and J. C. Light, On Detailed Balancing and Statistical Theories of Chemical Kinetics, *J. Chem. Phys.*, 1965, **42**, 3281–3291.

49 P. Pechukas, J. C. Light and C. Rankin, Statistical Theory of Chemical Kinetics : Application to Neutral-Atom–Molecule Reactions, *J. Chem. Phys.*, 1966, **44**, 794–805.

50 R. Johnson, 2002.

51 G. de Wit, B. R. Heazlewood, M. S. Quinn, A. T. Maccarone, K. Nauta, S. A. Reid, M. J. T. Jordan and S. H. Kable, Product state and speed distributions in photochemical triple fragmentations, *Faraday Discuss.*, 2012, **157**, 227–241.

52 F. Tureček and V. Hanuš, Mass spectra of ethenol and its deutero analogues, *Org. Mass Spectrom.*, 1984, **19**, 423–427.

53 G. Bouchoux, Keto-enol tautomers and distonic ions: The chemistry of [CnH2nO] radical cations. Part I, *Mass Spectrom. Rev.*, 1988, **7**, 1–39.

54 D. R. Yarkony and H. F. Schaefer, The acetyl cation and its geometrical isomers, *J. Chem. Phys.*, 1975, **63**, 4317–4328.

55 D. A. Blank, S. W. North, D. Stranges, A. G. Suits and Y. T. Lee, Unraveling the dissociation of dimethyl sulfoxide following absorption at 193 nm, *J. Chem. Phys.*, 1997, **106**, 539–550.

56 K. Huber, *Molecular spectra and molecular structure: iv. constants of diatomic molecules.*, Springer-Verlag, New York, 2013.

57 P. L. Houston and S. H. Kable, Photodissociation of acetaldehyde as a second example of the roaming mechanism, *Proc. Natl. Acad. Sci.*, 2006, **103**, 16079–16082.

58 F. A. L. Mauguière, P. Collins, Z. C. Kramer, B. K. Carpenter, G. S. Ezra, S. C. Farantos and S. Wiggins, Roaming: A Phase Space Perspective, *Annu. Rev. Phys. Chem.*, 2017, **68**, 499–524.

59 F. A. L. Mauguière, P. Collins, G. S. Ezra, S. C. Farantos and S. Wiggins, Multiple transition states and roaming in ion–molecule reactions: A phase space perspective, *Chem. Phys. Lett.*, 2014, **592**, 282–287.

60 F. A. L. Mauguière, P. Collins, G. S. Ezra, S. C. Farantos and S. Wiggins, Roaming dynamics in ion-molecule reactions: Phase space reaction pathways and geometrical interpretation, *J. Chem. Phys.*, 2014, **140**, 134112.

61 S. J. Klippenstein, Y. Georgievskii and L. B. Harding, Statistical Theory for the Kinetics and Dynamics of Roaming Reactions, *J. Phys. Chem. A*, 2011, **115**, 14370–14381.

62 H. E. Audier and T. H. Morton, Rearrangements in metastable ion decompositions of protonated propylamines, *Org. Mass Spectrom.*, 1993, **28**, 1218–1224.

63 A. W. Potts and W. C. Price, The Photoelectron Spectra of Methane, Silane, Germane and Stannane, *Proc. R. Soc. Math. Phys. Eng. Sci.*, 1972, **326**, 165–179.

Figures

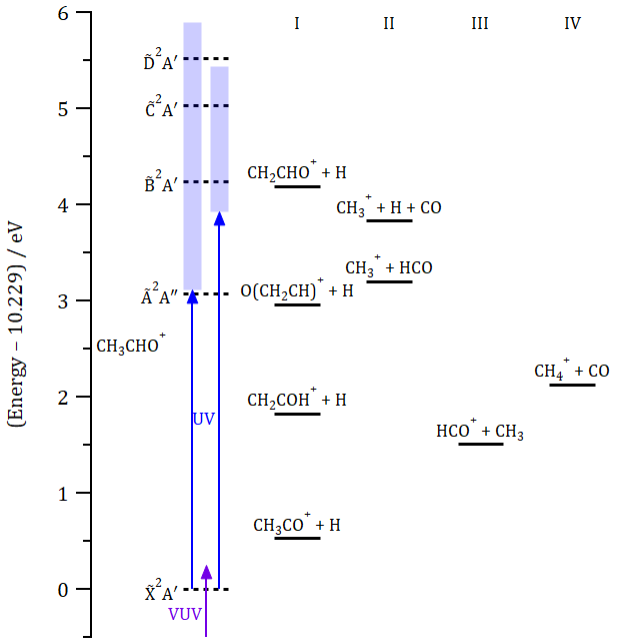

Figure 1 Schematic energy diagram for acetaldehyde cation photolysis. The shaded blue regions represent the photolysis wavelengths used for photofragment ion yield spectra (390–210 nm) and for ion images (316–228 nm). Excited state vertical excitation energies (dashed) are from EOM-CC(2,3)/cc-pVTZ calculations.

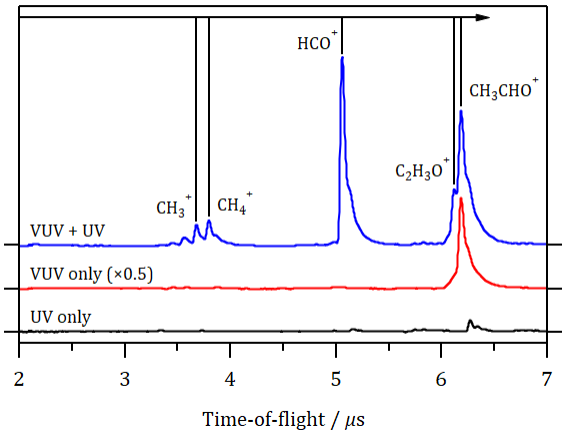

Figure 2. One-color and two-color time-of-flight mass spectra of CH_3CHO: (black) 308 nm UV photolysis pulse only; (red) 118.2 nm VUV ionization pulse only; (blue) both VUV + UV pulses. The time delay between the VUV and UV pulses was ~120 ns.

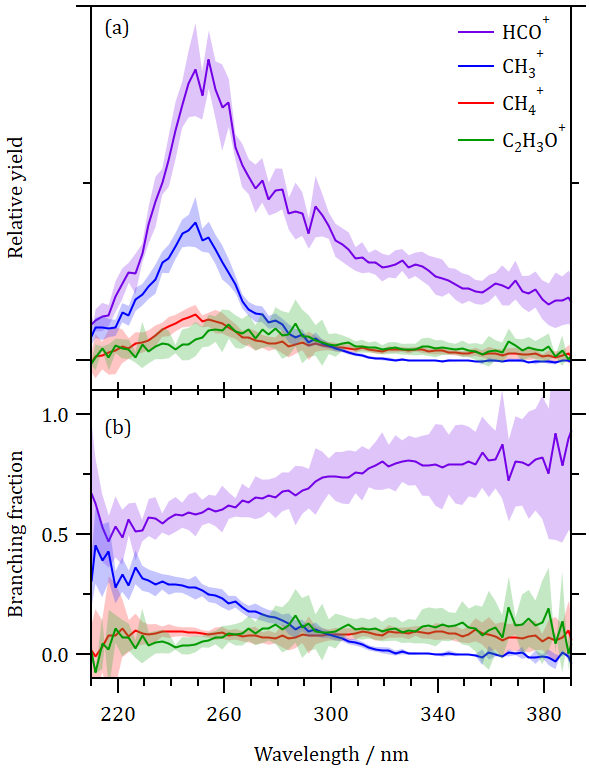

Figure 3 (a) CH_3CHO^+ PHOFY spectra recorded detecting $C_2H_3O^+$ (green), HCO^+ (purple), CH_4^+ (red), and CH_3^+ (blue); (b) branching fractions for each ionic photofragment.

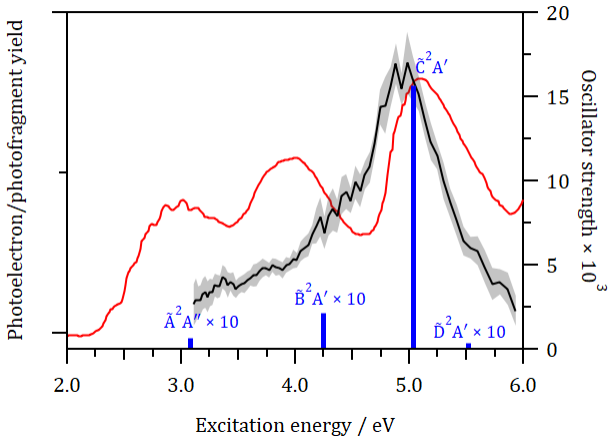

Figure 4 Total photofragment ion yield (black), photoelectron spectrum measured by Cvitaš *et al.*[28] (red), and oscillator strengths from EOM-CC(2,3)/cc-pVTZ calculations vs. vertical excitation energies (blue). Excitation energies are measured relative to the ground state of the CH_3CHO^+ cation; the photoelectron spectrum has been shifted by –10.23 eV.

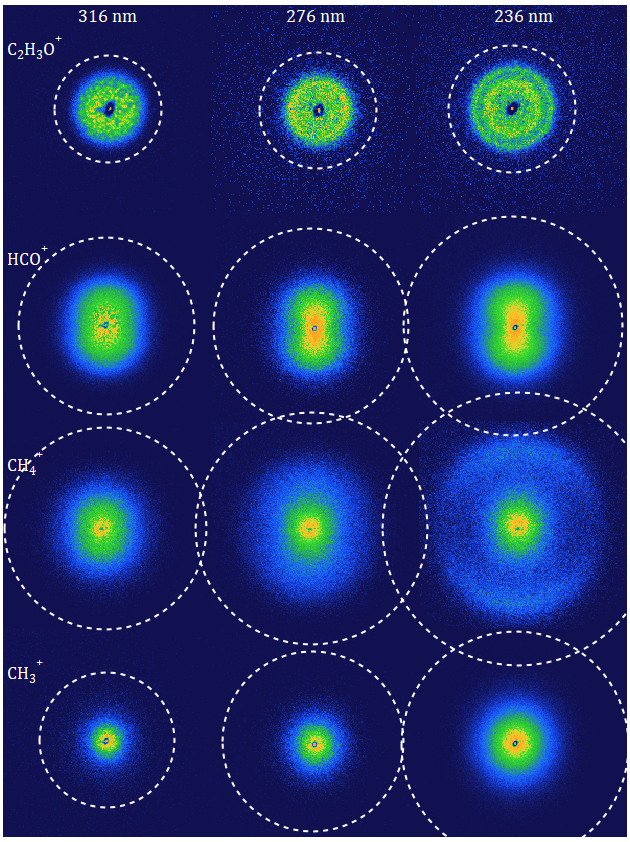

Figure 5 $C_2H_3O^+$, HCO^+, CH_4^+, and CH_3^+ ion images (top to bottom) following photolysis of CH_3CHO^+ at 316 nm, 276 nm, and 236 nm (left to right). Dashed circles represent the maximum possible speeds for each ionic fragment assuming the neutral co-fragments given in reactions I–IV. The $C_2H_3O^+$ images on the top row have been magnified by a factor of two to more clearly show the structure.

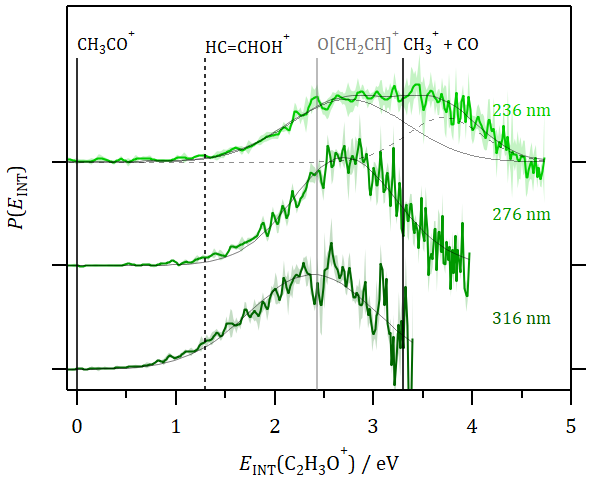

Figure 6 $C_2H_3O^+$ E_{INT} distributions at 316 nm, 276 nm, and 236 nm. Vertical lines are the energetic thresholds for formation of CH_3CO^+ isomers 1-hydroxyvinylium (dashed black) and vinoxyium (solid gray), along with secondary dissociation of $CH_3CO^+ \rightarrow CH_3^+ + CO$ (solid black). Total fits are shown (solid black) along with individual components of the 236 nm E_{INT} distribution (solid and dashed black). The dashed component corresponds to formation of the 1-hydroxyvinylium isomer.

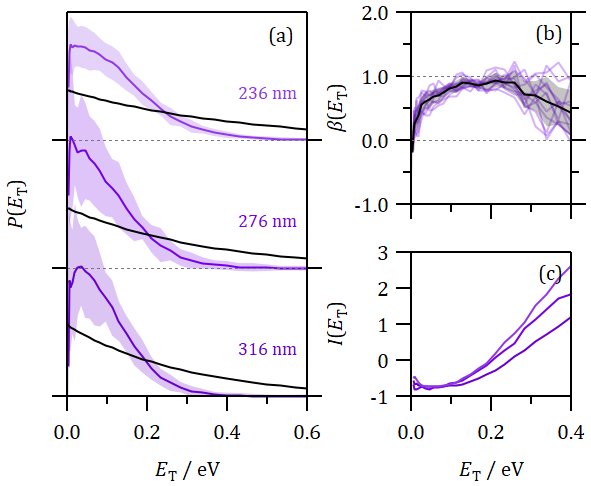

Figure 7 (a) HCO^+ total translational energy distributions at 316 nm, 276 nm, and 236 nm; (b) $\beta(E_T)$ are shown for all photolysis wavelengths (316 – 228 nm) along with their average (black); (c) linear surprisal plots showing two distinct gradients.

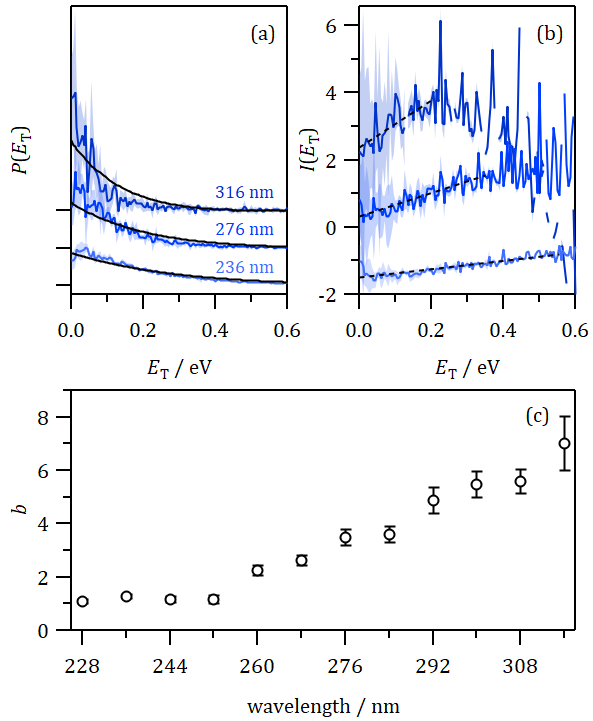

Figure 8 (a) CH_3^+ total translational energy distributions and phase space theory calculations (black) at selected photolysis wavelengths of 316 nm, 276 nm, and 236 nm; (b) linear surprisal plots; (c) variation of surprisal parameter, *b*, with available energy.

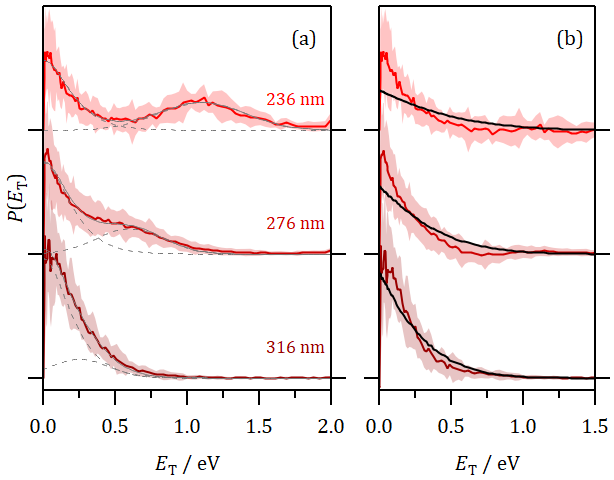

Figure 9 (a) CH_4^+ total translational energy distributions at selected photolysis wavelengths of 316 nm, 276 nm, and 236 nm along with total fits (solid gray) and individual fits (dashed gray); (b) Isolated slow component after subtraction of the fast component shown alongside PST calculations (solid black).

Tables

Table 1 Summary of CH_3CHO^+ electronic states and ejected electron characters. Experimental vertical ionization energies (IE) are taken from the photoelectron spectroscopy work of Yencha *et al*.[31] and calculated values are at the EOM-CC(2,3)/cc-pVTZ level. Threshold wavelengths for excitation are relative to the ground state of the ion.

State	Character	Expt. IE [Calc. IE]/ eV	λ / nm
$\tilde{X}^2A'$	n_O (10a′)	10.228 [10.574]	
$\tilde{A}^2A''$	$\pi_{C=O}$ (2a′)	13.09 [13.651]	403
$\tilde{B}^2A'$	π_{CH_3} (9a′)	13.93 [14.818]	292
$\tilde{C}^2A'$	σ_{C-C} (8a′)	15.20 [15.606]	246
$\tilde{D}^2A'$	π_{CH_3} (1a″)	15.5 [16.095]	225

Table 2 Dissociation energies (D_0), appearance energies (AE), and threshold wavelengths (λ_{th}) for various fragment ions.[32] D_0 values are calculated from 0 K thermodynamic data obtained from the Active Thermochemical Tables (ATcT).[47] Uncertainties are < 8 meV. Appearance energies, AE and ΔAE, are from Jochims *et al*.[32] Also shown in parentheses are ΔD_0 and ΔAE, the dissociation and appearance energies relative to the zero-point level of CH_3CHO^+.

Ion	D_0 (ΔD_0)/ eV	λ_{th} / nm	AE (ΔAE) / eV	λ_{th} / nm
$C_2H_3O^+$	10.758 (0.528)	2348	10.90 (0.67)	1850
HCO^+	11.739 (1.510)	821	12.03 (1.80)	689
CH_4^+	12.356 (2.126)	583	12.61 (2.38)	521
CH_3^+	13.429 (3.200)	387	14.08 (3.85)	322
CO^+	13.751 (3.521)	352	–	–